Improving the thermoelectric performance of scandium nitride thin films by implanting helium ions

Hugo Bouteiller, Razvan Burcea, Charlotte Poterie, Danièle Fournier, Fabien Giovannelli, Johan Nyman, Younès Ezzahri, Sylvain Dubois, Per Eklund, Arnaud Le Febvrier, et al.

communications materials

Article

https://doi.org/10.1038/s43246-025-00741-2

Improving the thermoelectric performance of scandium nitride thin films by implanting helium ions

Hugo Bouteiller[1,7] ✉, Razvan Burcea[1,2], Charlotte Poterie[1], Danièle Fournier[3], Fabien Giovannelli[4], Johan Nyman[5,8], Younès Ezzahri[1], Sylvain Dubois[1], Per Eklund[5,6], Arnaud le Febvrier[5,6] ✉ & Jean-François Barbot[1] ✉

Ion implantation is a widely used technique to introduce defects in low-dimensional materials and tune their properties. Here, we investigate the thermoelectric properties of scandium nitride thin films implanted with helium ions, revealing a positive impact of defect engineering on thermoelectric performance. Transport properties modeling and electron microscopy provide insights on the defect distribution in the films. The electrical resistivity and Seebeck coefficient increase significantly in absolute values after implantation and partially recover upon annealing as some of the implantation-induced defects heal. The thermal conductivity decreases by 46 % post- implantation due to the formation of extended defects and nanocavities. Consequently, the thermoelectric figure of merit zT doubles for the sample annealed at 673 K. These findings highlight the potential of controlled ion implantation to enhance thermoelectric properties in thin films, paving the way for further optimization through defect engineering.

Transition metal nitrides (TMNs) thin films have been widely studied in the past decades for a wide range of applications[1–5], taking advantage of their excellent mechanical[6,7], plasmonic[8,9], piezoelectric[10,11] and, more recently unveiled, thermoelectric properties[11–13]. Among them, ScN was extensively investigated as it exhibits a semiconducting behavior with an indirect bandgap of 0.9 eV and direct bandgap of 2.2 eV[14–19], a high hardness of 21 GPa[20], a substantial wear corrosion resistance and an elevated melting point standing above 2600 °C[11,21]. Unlike conventional III-V nitride semiconductors, ScN crystallizes in a NaCl structure-type with an octahedral Sc coordination, leading to N 2*p* orbital dominance at the top of the valence band and predominant Sc empty 3*d* t_{2g} states at the bottom of the conduction band[22–25]. While it is well known that native defects such as N vacancies and incorporated impurities like O_N substitutions can alter the electronic band structure, it turns out that the latter is relatively rigid[25]. Consequently, such defects only impact the position of the Fermi level, freely shifting towards valence or conduction bands depending on the nature of the doping. As N vacancies or unwanted impurities like O or F act as electron donors, the Fermi level lies in the conduction band, leading to *n*-type degenerate semiconducting behavior in most sputter-deposited ScN films. The reported carrier densities fall in the 10^{18} – 10^{22} cm^{-3} range, mainly depending on the O at. % incorporated during deposition[22,25–28]. Unwanted O impurities are hardly avoidable, owing to both a low, negative O_N formation energy, and a high affinity of Sc with O[24].

In the last decade, a number of studies have proved ScN to be a promising low dimensional thermoelectric material[13,23,26–31]. Thermoelectric materials allow the direct conversion of thermal energy into electricity using the Seebeck effect, the process being reversible[32]. The thermoelectric performance of such materials is assessed by the figure of merit $zT = S^2T/\rho(\kappa_e + \kappa_L)$, S being the Seebeck coefficient, ρ the resistivity, κ_e the electronic thermal conductivity, κ_L the lattice contribution to the thermal conductivity and T the absolute temperature. The improvement of the figure of merit often arises from a reduction of the thermal conductivity while maintaining favorable electrical transport properties through a maximized power factor $PF = S^2/\rho$[32]. The reported power factors for *n*-type ScN are as high as 2–4 $mW{\cdot}m^{-1}{\cdot}K^{-2}$ at about 800 K[13,23,26–28,30,31], competitive with current state-of-the-art materials such as Bi_2Te_3[33], PbTe[34], or SiGe[35] in their

[1]PPRIME Institute, CNRS, Université de Poitiers–ENSMA, UPR 3346, SP2MI, TSA 41123, 86073, Poitiers, cedex 9, France. [2]Université Paris-Saclay, CentraleSupélec SPMS, F-91192 Gif-sur-Yvette, France. [3]Institut des NanoSciences de Paris, Sorbonne Université, UFR 925, UMR 7588, Paris, F-75005, France. [4]Laboratoire GREMAN, CNRS, Université de Tours, UMR 7347, 41029 Blois, France. [5]Department of Physics, Chemistry and Biology (IFM), Linköping University, SE-581 83 Linköping, Sweden. [6]Inorganic Chemistry, Department of Chemistry – Ångström, Uppsala University, Box 538, SE-751 21 Uppsala, Sweden. [7]Present address: Materials Science and Technology Division, Oak Ridge National Laboratory, Oak Ridge, TN, 37831, USA. [8]Present address: Husqvarna AB SE-561 82, Huskvarna, Sweden. ✉e-mail: bouteillerh@ornl.gov; arnaud.lefebvrier@kemi.uu.se; jean.francois.barbot@univ-poitiers.fr

respective temperature range. The thermal conductivity of ScN, however, is relatively high with a value of about 12 $W{\cdot}m^{-1}{\cdot}K^{-1}$ at room temperature, preventing ScN to exhibit competitive zT values so far (0.2–0.3 at 800 K)[11,13,22,31]. Attempts to reduce the thermal conductivity was conducted by alloying ScN with several metals such as Mg or Nb but resulted in either no thermal conductivity reduction (Mg doping)[30] or degradation of electrical properties (Nb doping)[36], preventing further zT improvements.

An effective way to reduce the thermal conductivity is to introduce defects in the material. That can be done by taking advantage of the ion implantation technique in low dimensional materials. The ion implantation process is particularly interesting for thermoelectric outcomes as it leverages from two beneficial synergistic effects: (i) the fine tuning of the charge carrier concentration by controlling the implanted dopant doses, and (ii) the reduction of the lattice thermal conductivity through phonon scattering by inducing point defects or nanocavities. Studies conducted on implanted/irradiated nanosized silicon, where the nature and behavior of generated defects are well understood, have demonstrated that these defects can effectively reduce or even control the lattice thermal conductivity[37,38]. Furthermore, this technique has already proved to be truly promising to improve thermoelectric properties, as recently reported[39–46].

The thermoelectric properties of irradiated and implanted ScN with different ions were investigated in recent years. Tureson et al. have implanted Mg^{+} in (111) ScN grown on c-sapphire substrate, where a notable threefold thermal conductivity reduction was observed after room-temperature implantations[47]. An irradiation of ScN thin films by Li+ ions was conducted by Rao et al., yielding a halved thermal conductivity in the 300–950 K temperature range[46]. The power factor was maintained at a decent value of about 1–2 $mW{\cdot}m^{-1}{\cdot}K^{-2}$, resulting in an overall preserved figure of merit. More recently, an implantation of non-electrically active argon ions into ScN thin films at room temperature resulted in a drastic reduction of the thermal conductivity, from 12.5 to 3 $W{\cdot}m^{-1}{\cdot}K^{-1}$ at 300 K for as-implanted samples[45]. The use of heavy noble gas ion was motivated by the large ballistic effects providing both point defects and extended defects[48]. Noble gas are indeed known to form complex-like defects with atomic vacancies[49–51], further adding scattering centers for phonons and thus having a strong impact on the lattice thermal conductivity. Complex-like defects result from the aggregation of vacancies, leading to vacancies clusters which are stabilized by the presence of implanted helium atoms[50]. The electrical transport properties were strongly impacted, and subsequent high temperature annealing revealed a partial recovery of the defects, demonstrating the extensive impact of defect recombination on the transport properties[45].

Ion implantation has shown potential as an effective technique for enhancing thermoelectric properties by introducing defects in materials, although the specific mechanisms governing these improvements remain to be fully elucidated. Building on previous work with argon-implanted ScN thin films[45], we extend this investigation to helium, a lighter noble gas. Given the significant differences in mass and radius between argon and helium, differences in implantation-induced defects and their subsequent effects on transport properties could be expected. SRIM simulations confirm that each argon ion creates over ten times more vacancies than helium ions, suggesting that the lighter helium could lead to distinct defect characteristics and thermal behavior.

In this study, we investigate the electrical and thermal transport properties of helium-implanted ScN thin films, with a particular focus on the stability of implantation-induced defects under different annealing conditions. By correlating these properties with microstructural changes observed through electron microscopy, we aim to shed light on how helium implantation affects defect formation and recovery. Ultimately, we identify the optimal annealing process that maximizes the thermoelectric performance of ScN films, providing new insights into the role of defect engineering in enhancing material properties for thermoelectric applications.

Results and discussion

According to ERDA characterization, the composition of the as deposited film is estimated to be $ScN_{0.95(1)}$ with the presence of about 3.5(2) at. % oxygen content. At this doping level, a degenerate semiconducting behavior is expected due to the shifting of the Fermi level in the conduction band. Structural characterizations by means of Transmission Electron Microscopy (TEM) were carried out on the reference sample as shown in Fig. 1, and confirmed the epitaxy of the (111) oriented ScN film on the (0001) Al_2O_3 substrate, including the presence of twins due to the epitaxial relation between the film and the substrate. Further details on the microstructure of the reference film are reported in a previous study[45].

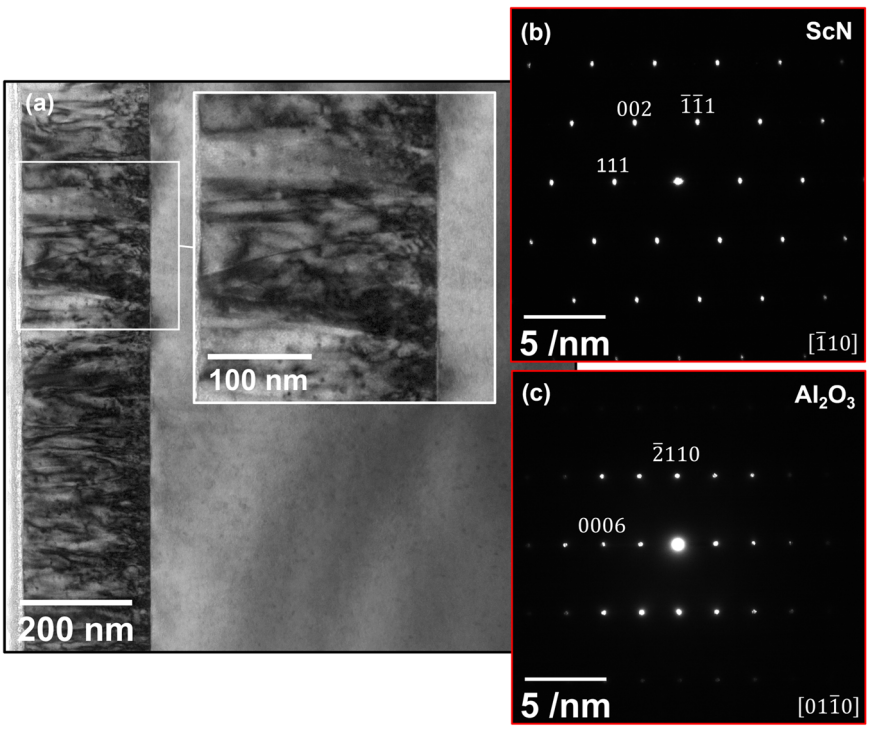

Fig. 1 | Transmission Electron Microscopy of a reference scandium nitride film deposited on a *c*-sapphire substrate. a Bright field TEM micrograph of a reference sample of ScN thin film deposited on a Al_2O_3 substrate. The columnar nature of the two growth variant type grains can be observed in the inset **a**. Electron diffraction patterns of both ScN and Al_2O_3 are displayed in the inset **b** and **c**, respectively, confirming the epitaxy relationship between the film and the substrate.

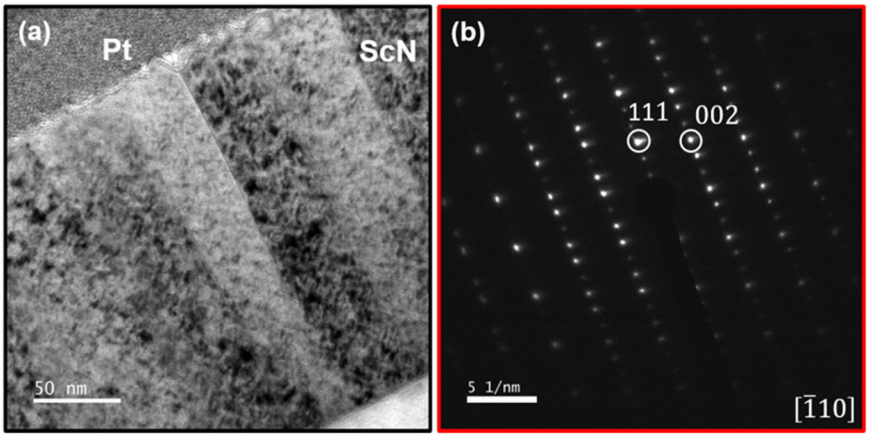

Fig. 2 | Transmission Electron Microscopy micrograph of the helium-implanted film of scandium nitride deposited on *c*-sapphire substrates. a Bright field micrograph, **b** Electron Diffraction pattern of the area along the zone axis [1̄10].

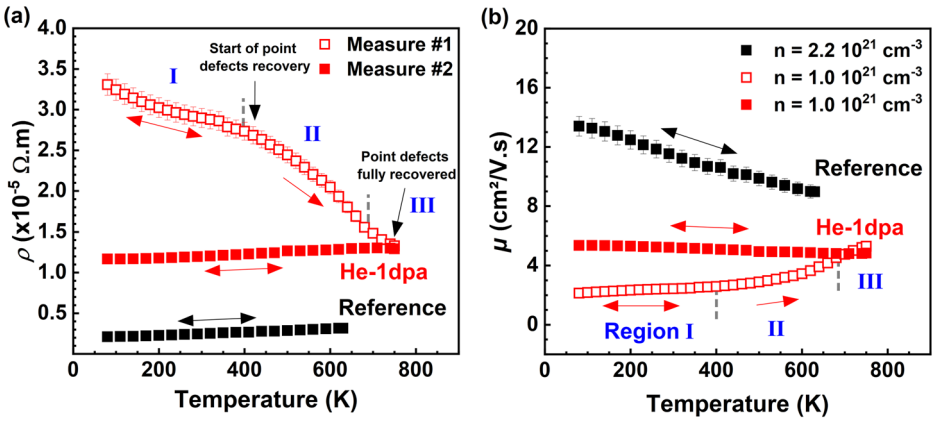

Fig. 3 | Influence of helium implantation and subsequent in-situ annealing on the electronic transport properties of a scandium nitride film. Resistivity (**a**) and charge carrier mobility (**b**) measurements of the ScN reference and He-implanted films. Point-like defects induced by implantation of He ions are recovered when a temperature of approx. 750 K is reached, similar to Ar-implanted ScN thin films[43]. The charge carrier concentration were measured to be constant over the whole temperature range. Double arrows indicate that the measurements are reversible while single arrows characterize irreversible measurements due to partial defect recovery. Standard deviations are 4% and 5% for the resistivity and mobility, respectively.

Figure 2 presents a TEM micrograph of the ScN film implanted with He ions at a damage level of 1 displacement per atom (dpa). Diffuse black dots can be observed, suggesting the presence of He implantation-induced defects. The diffraction picture recorded from this micrograph indicates that no part of the sample was amorphized, the crystallinity of the film being preserved as shown by the well-defined diffraction spots and the absence of amorphous rings (Fig. 2b). The columnar nature of the film grains is also maintained, with well-defined grain boundaries, despite the clear presence of defects.

Figure 3 presents the temperature dependence of electrical resistivity and mobility for both reference and helium-implanted ScN films. As expected, the reference sample exhibits metallic conductive behavior, typical of a degenerate semiconductor, due to high doping levels resulting from the presence of oxygen impurities. The charge carrier concentration remains constant throughout the temperature range, with a value of $2.2(2) \times 10^{21}\,cm^{-3}$, consistent with previously reported studies on ScN films grown under the same conditions[45,48]. After helium implantation, a notable shift in conduction mode was observed, with the resistivity decreasing as temperature increases—a behavior also seen in argon-implanted films with the same damage level (1 dpa)[48].

Two types of defects emerged after helium implantation: point-like defects and complex-like defects. The data in Fig. 3 shows two measurements from 80 K to 750 K performed successively, the second measurement thus being conducted after an in situ annealing at 750 K, a temperature where the point-like defects have recovered. In region I (Measure #1, $T < 400$ K), the resistivity and mobility are cyclable, indicating that point-like defects concentration remains constant. As the temperature exceeds 400 K (region II, $400\ K < T < 720$ K), point defects start to recover, resulting in irreversible changes to transport properties. At temperatures above ~720 K (region III), only complex-like defects remain and dominate the resistivity and mobility. Once the point defects have fully recovered, metallic-like behavior is restored, as seen in the second set of measurements (Measure #2, Fig. 3a). In region I, both point-like and complex-like defects influence transport, while in region III, only complex-like defects remain active. Point-like defects mainly affect the conduction mechanism, whereas complex-like defects act as charge trapping. Indeed, the charge carrier concentration remains constant at $1.0(2) \times 10^{21}\,cm^{-3}$ across the 80–750 K range, indicating that the ~50% reduction in carrier density results exclusively from complex-like defects: point-like defects do not act as carrier traps[45,48]. The point defects only affect the conduction mechanism and also contribute to a decrease in electron mobility (Fig. 3b)[48].

These findings indicate that helium implantation has similar effects on transport properties as those observed previously with argon implantation, in particular concerning the changes in conduction mode[48]. It should be noted that despite substantial differences in concentration (0.05% for Ar and 1% for He) and atomic mass (40.0(1) AMU for Ar and 4.0(1) AMU for He) between the two studies, the nature of the implantation-induced defects remains quite similar. On the other hand, these experiments were conducted at the same damage level of 1 dpa. Therefore, the influence of ion implantation on the electrical transport properties appears to be primarily governed by the level of damage introduced in the material rather than the quantity/type of the noble gas implanted.

To further understand the conduction mechanism, the resistivity was plotted as $\ln(\rho) = f(1/T)$ (Fig. 4a) and $\ln(\rho) = f(1/T^{1/4})$ (Fig. 4b) and different models were fitted and compared with the literature. The as-implanted resistivity can be fitted with an Arrhenius law in the region II (Fig. 4a), yielding an activation energy of the point-defect recombination of 130(10) meV. That value is slightly larger than the activation energy of the point defect recombination generated by Ar or Mg implantation ions

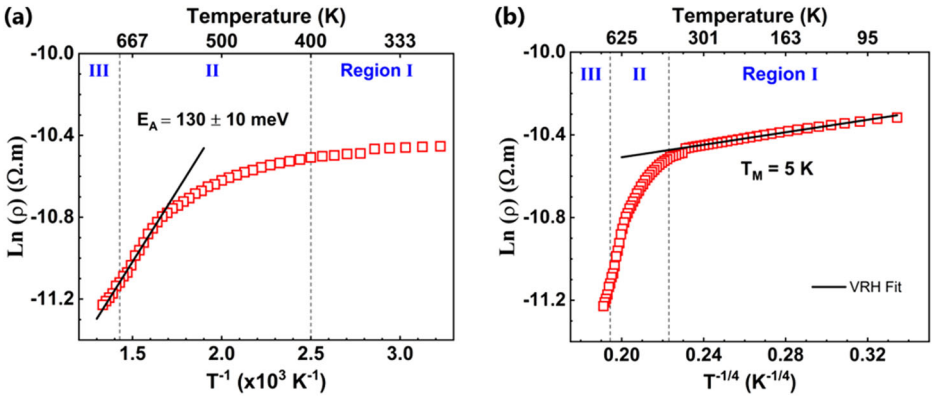

Fig. 4 | Fitting curves of helium-implanted films during the first measurement where point-like defects are being recovered upon heating. **a** $\ln(\rho) = f(1/T)$, yielding an energy activation of the defect recovery process of $E_A = 130$ meV, **b** $\ln(\rho) = f(1/T^{1/4})$, fitted using a Mott law, unveiling a Variable Range Hopping (VRH) conduction behavior with a Mott temperature of $T_M = 5$ K.

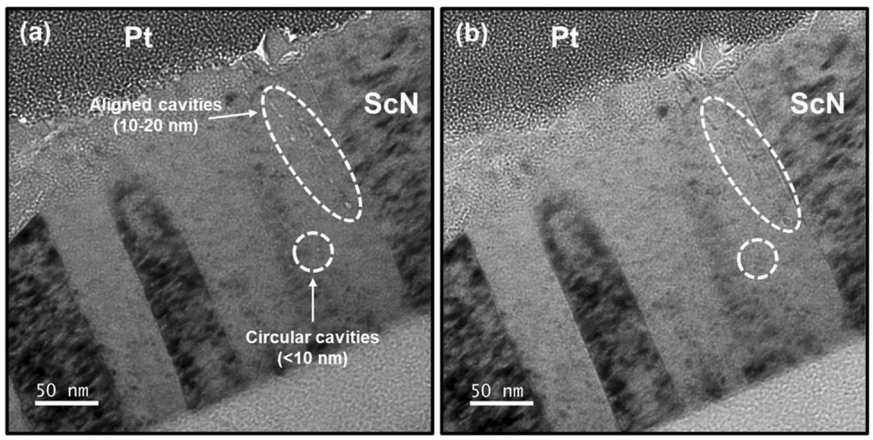

Fig. 5 | Transmission Electron Microscopy micrographs of helium-implanted films on *c*-sapphire substrates (no annealing). **a** Under-focused and **b** over-focused bright field micrographs, unveiling the presence of nanocavities (5–20 nm) induced by He species on the as-implanted sample. The cavities are aligned with the grain growth, suggesting that their formation is favored in the grain boundaries regions.

(about 90 meV for both)[47,48]. In addition, the fitting of the ln (ρ) = f($1/T^{1/4}$) curve in the low temperature range (region I) with a Variable Range Hopping model as proposed by Mott and Davis[52], yielded a Mott temperature of $T_M = 5$ K (Fig. 4b). This value is in the same order of magnitude than that of Ar-implanted ScN films with an equivalent damage level of 1 dpa ($T_M = 1$ K). According to Mott's model, the Mott temperature is related to the localization parameter L_c of the defects as $T_M \sim A/(N_F L_c^3)$, (A being a constant and N_F the density of states at the Fermi level). Consequently, the increase in the Mott temperature suggests a decrease in the localization parameter L_c, calculated to be approximately 36 nm based on an estimated density of states N(E_F) of about 10^{21} $eV^{-1}{\cdot}cm^{-3}$, according to the calculations of the position of the Fermi level by Mu et al.[53]. Hence, it can be deduced that the He-implanted films exhibit a slightly larger defect density than Ar-implanted films despite the large difference in gas concentration. This is consistent with the fact that the Mott temperature increases with the fluence, hence with the number of implanted ions and generated defects[54]. Conversely, T_M is reduced when the film undergoes an in situ annealing (between 400 K and 750 K) due to the recombination of the defects. These differences motivated further investigation into the microstructural properties of the He-implanted ScN.

TEM micrographs of the as-implanted ScN film with helium ions in bright field, out of zone axis and in Fresnel conditions are presented in Fig. 5. By playing with the focus, the presence of nanocavities of about 10–20 nm, eventually resulting from He bubbles, can be detected. Such cavities are dispersed along the growth direction, suggesting that these inclusions are favored near the grain boundaries. These cavities are thus formed in the He as-implanted ScN films, while being only observed after high-temperature annealing in the case of Ar-implanted ScN[45]. Noble gases are known to form complexes with vacancies within implanted solids, forming voids or bubbles upon aggregation that occurs either during implantation or upon post-implantation thermal treatment[55]. It is reasonable to assume that the formation of vacancy-noble gas complexes is favored in the case of He due to (i) the large number of available vacancies and the mobility of helium (lower atomic radius $r_{He} = 0.31$ Å compared to $r_{Ar} = 0.71$ Å), and (ii) the concentration of He ions used (~1%) being 20 times larger than that of Ar (~0.05%) for an equivalent level of damage (1 dpa). The presence of such complexes, which are considered precursors to cavity formation and are favored near grain boundaries, accounts for the formation of nanometric cavities in these regions.

The presence of nanocavities in the film after He-implantation are expected to have a significant impact on thermal properties, as nanoinclusions are well-known to act as scattering centers for phonons[56]. Furthermore, annealing the sample at high temperatures is anticipated to affect these cavities through thermally activated diffusion mechanisms. Figure 6 shows a TEM micrograph of the He-implanted sample annealed at 1273 K. After high temperature annealing, the nanocavities remain present with a notable increase in size, evidenced by the presence of larger, aggregated cavities of approximately 40 nm (compared to 5–20 nm before annealing). Their formation is still favored along the grain growth direction explained by an easier diffusion along the grain boundaries.

The investigation of the complete transport properties of the as grown and annealed implanted ScN films with different thermal treatment is presented in the following sections to assess the influence of such inclusions and their thermal history on the thermoelectric properties.

The temperature dependence electrical resistivity and the electron mobility from the reference ScN film, He-implanted and annealed at various temperatures samples are depicted in Fig. 7. The so-called in situ annealing sample refers to the sample measured once up to 750 K (Fig. 3). The electron mobility of the 750 K in situ annealed (few seconds) film and the 673 K annealing (10 min) film are very similar, the slight differences between these

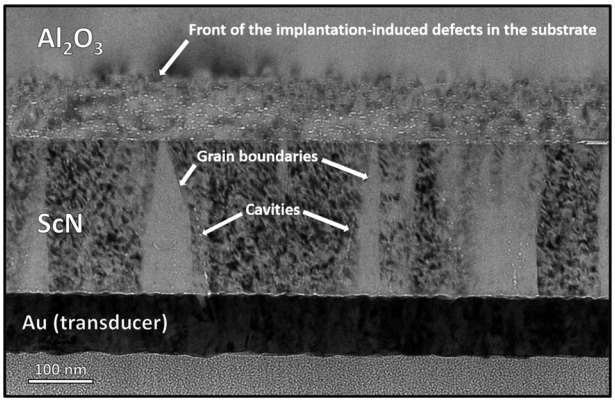

Fig. 6 | Transmission Electron Microscopy micrographs of a helium-implanted film annealed at 1273 K. Bright field micrographs under 3-waves configuration, showing the presence of the He-implantation-induced nanocavities. The cavities distribution in the film is still aligned along grain boundaries. However, the density of nanocavities has increased compared to the as-implanted sample.

two samples being attributed to the kinetics of defect recovery. Annealing at higher temperatures (1273 K) provokes a recovery of complex-like defects, leading to further recovery of the electrical resistivity and carrier concentration close to those of the reference film. Despite the recovery of charge carrier concentration, the electron mobility remained unchanged compared to the in situ annealed sample. The reduced and unchanged mobility of the annealed samples suggested that residual microstructural defects, such as cavities (Figs. 5 and 6), persist in the sample and act as scattering centers for electrons.

To understand further the scattering mechanism resulting from the presence of such cavities and nanostructure, a modeling of the mobility curves was performed according to the Matthiessen law displayed in Eq. (1) with $\mu(T)$ the temperature dependent mobility, and $\mu_{Latt}(T)$, $\mu_{GB}(T)$, μ_R, and μ_D the lattice, grain boundaries', residual impurities' and implantation-induced defects' contributions to the mobility, respectively.

$$\frac{1}{\mu(T)} = \sum_i \mu_i = \frac{1}{\mu_{Latt}(T)} + \frac{1}{\mu_{GB}(T)} + \frac{1}{\mu_R} + \frac{1}{\mu_D} \quad (1)$$

The fitting of the as-grown reference ScN curve indicates that the electron mobility is primarily driven by electron-phonon interactions ($\mu_{Latt}(T) = \beta\, T^{-3/2}$) and residual impurities ($\mu_R = 14 - 15$ cm^2·V^{-1}·K^{-1}). The grain boundaries ($\mu_{GB}(T)$) appeared to be negligible, which is consistent with a recent study on the electron mobility in ScN[57]. The implantation of He results in a drastic reduction in mobility, which becomes almost constant over temperature (Fig. 8). The modeling of this curve could be accurately carried out adding a supplementary term in the Matthiessen's law ($\mu_D = 8 - 9$ cm^2·V^{-1}·K^{-1}), which dominates the mobility scattering mechanisms. High-temperature annealing at 1273 K results in a slight increase in this value ($\mu_D^{1273} = 10 - 11$ cm^2·V^{-1}·K^{-1}) and alters the lattice mobility pre-factor (β). This is consistent with the structural changes and their evolution upon subsequent annealing observed by TEM analysis. Hence, the presence of nanocavities and localized defects play a dominant role in the charge carriers scattering mechanism and explains well the large reduction in mobility observed after implantation of helium species. This dominant contribution might be enhanced by the surface of the nanocavities as it was shown that the edges of nanocavities under the form of pores are dominating the scattering mechanism of electrons[58].

The Seebeck coefficient and power factor are displayed in Fig. 8. The absolute values of the Seebeck coefficient for all samples increase linearly with temperature, which is consistent with the degenerate semiconductive behavior. The absolute Seebeck coefficient of the He-implanted sample was doubled on the whole temperature range, reaching −80 μV·K^{-1} at 673 K, compared to −46 μV·K^{-1} for the reference at the same temperature. It can be noted that the absolute value of the slope is increased by about 80% after implantation and an in situ annealing at 750 K (red data in Fig. 8. This observation is consistent with the decrease of the charge carrier concentration after implantation which was halved. A decrease in the slope of the Seebeck coefficient was also observed in the case of Ar-implanted ScN films, the latter being however more pronounced (decrease by a factor of 3) while the charge carrier concentration was also halved after implantation[45]. This little difference might be explained by the fact that the complex-like defects arising from the coupling of vacancies with the noble gas ($NG_n\ V_m$, $n < m$, NG = Ar, He), although similar in nature, induce a slightly different effect on the density of states and therefore on the electrical properties of the film. Helium atoms, trapped by the vacancy complexes, are present in a substantially higher quantity than in the case of argon implantations, due to the higher implanted concentration of the former compared to the latter. Therefore, the defects generated in the case of He are expected to have a more localized influence, which would lead to a less affected DOS near the Fermi level, explaining the slight difference in the Seebeck coefficient slopes when compared to Ar implanted ScN films[45]. A modest variation of the slope is observed after the annealing at 673 K, in line with the slightly decreased charge carrier concentration and mobility. However, the sample annealed at 1273 K exhibited comparable values as the reference sample. Interestingly, it can be noted that despite the very limited recovery of mobility and partial recovery of resistivity, the Seebeck coefficient is fully recovered, same as the charge carrier concentration. This result might be attributed to the fact that the density of states (DOS) near the Fermi level is not significantly modified, leading to a similar electron effective mass between the reference and the high-temperature annealed sample. On the other hand, the presence of larger size, aggregated cavities and nano-inclusions as observed in TEM micrographs after high-temperature annealing are responsible for the strong reduction of the mobility, leading to an overall increased resistivity. The resulting power factor of all samples are presented in Fig. 8. Due to resistivity rises, the power factor of the 750 K in situ annealed sample and the 1273 K annealed sample is lowered by about 18% and 42% at 600 K, respectively. However, the sample annealed at 673 K presents a very similar power factor than that of the reference film,

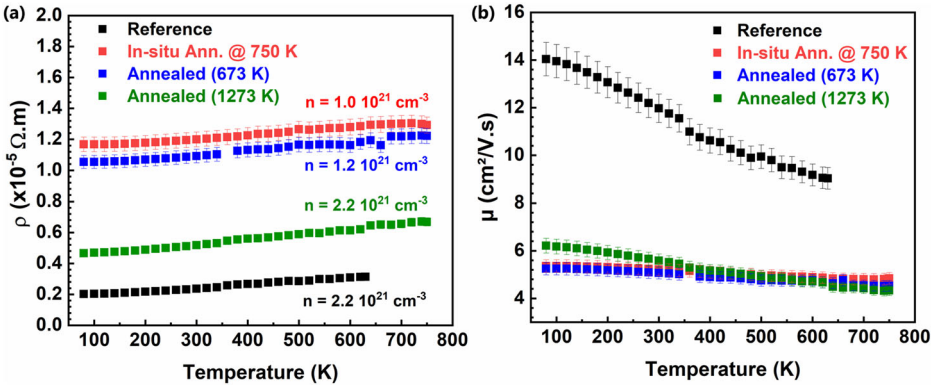

Fig. 7 | Electronic transport properties of scandium nitride films annealed in different conditions. a Resistivity and **b** mobility curves of the ScN Reference (black), He-implanted and in-situ annealed at about 750 K (point-like defects recovered – red), He-implanted then annealed at 673 K (blue), and He-implanted then annealed at 1273 K (green) films. The charge carrier concentrations were measured to be constant over the whole temperature range. Standard deviations are 4% and 5% for the resistivity and mobility, respectively.

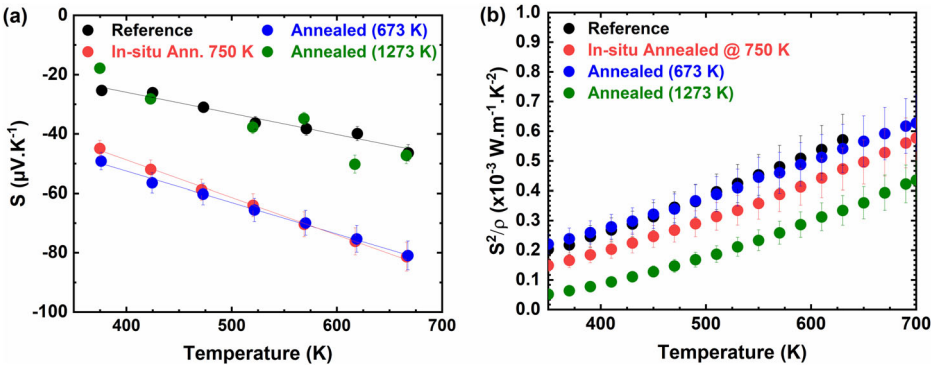

Fig. 8 | Seebeck coefficient and power factor of scandium nitride films annealed in different conditions. a Seebeck coefficient and **b** Power factor of the ScN reference (black), He-implanted after recovery of point-like defects (in situ annealing at about 750 K, red), He-implanted then annealed at 673 K (blue), and He-implanted then annealed at 1273 K films (green). Standard deviations are 6% and 15% for the Seebeck coefficient and the power factor, respectively.

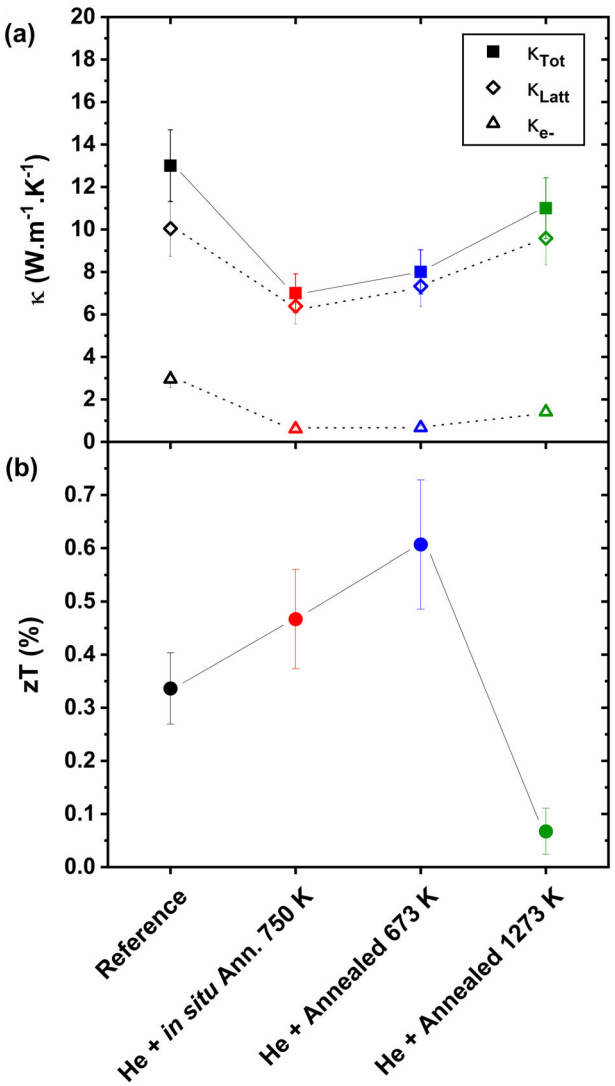

Fig. 9 | Thermal transport and thermoelectric figure of merit of scandium nitride films annealed in different conditions. a Thermal conductivity and **b** figure of merit zT of the Reference (black), He-implanted then in situ annealed at about 700 K (red), implanted then annealed at 673 K (blue), and implanted then annealed at 1273 K samples at room temperature (green). The lattice and electronic contributions to the thermal conductivity are displayed. Standard deviations are 13% and 20% for the thermal conductivity and zT, respectively.

suggesting that the microstructure of the sample at this stage, which includes small size nanocavities (about 5–20 nm), does not reduce the electrical transport properties performance.

The thermal conductivities of all samples were measured at room temperature using the modulated thermoreflectance technique. Detailed information on the fitting models of the thermoreflectance data and subsequent analysis can be found in the Methods section. The resulting thermal conductivities at room temperature are depicted in Fig. 9a, along with their lattice and electronic contributions. The reference sample exhibits a thermal conductivity of about 13(1) $W{\cdot}m^{-1}{\cdot}K^{-1}$, consistent with values reported in the literature[30,36,47]. Although the lattice thermal conductivity is dominant, the electronic contribution is significant (~23%) due to the degenerate semiconducting behavior, where free electrons substantially contribute to thermal transport. Upon implantation, the thermal conductivity is significantly reduced to a value of about 7(1) $W{\cdot}m^{-1}{\cdot}K^{-1}$, marking a 46% drop. This large decrease of the thermal conductivity after ion implantation is expected and has been previously reported in the literature[40,42–47,59]. In the present implanted ScN samples which were in situ-annealed at 750 K, annealed at 673 K and annealed at 1273 K, only complex-like defects and nanocavities are remaining in the films. As shown in Fig. 10a, both the lattice and electronic contributions to thermal conductivity are significantly impacted by those induced defects by ion implantation, acting as efficient scattering centers and strongly reducing the thermal conductivity. Complex-like defects, being much smaller than nanocavities (10–40 nm), predominantly scatter short-wavelength phonons, playing a dominant role in reducing the lattice thermal conductivity by effectively disrupting phonon transport within the grains[56,60]. In contrast, nanocavities scatter long-wavelength phonons due to their larger size. However, their contribution to lattice thermal conductivity reduction appears to be rather limited in this study. Despite the persistent presence of nanocavities after high-temperature annealing (1273 K), the lattice thermal conductivity is almost fully recovered at about 10.5(10) $W{\cdot}m^{-1}{\cdot}K^{-1}$, suggesting that long-wavelength phonons contribute minimally to overall phonon scattering in these sample series.

Nanoinclusions, on the other hand, have a more pronounced effect on the electronic thermal conductivity. After annealing at 1273 K, the electronic contribution remains halved (about 1.5 $W{\cdot}m^{-1}{\cdot}K^{-1}$) compared to the reference sample, consistent with significant charge carrier scatterings at nanoinclusion surfaces, reducing the carrier mobility. The recovery of the complex-like defects after high temperature annealing leads to a partial restoration of the thermal conductivity, up to $k \sim 10.5(10)$ $W{\cdot}m^{-1}{\cdot}K^{-1}$ for the sample annealed at 1273 K, as the scattering effects of these defects are suppressed. Overall, the cumulative effects of these scattering mechanisms lead to the observed strong reduction in thermal conductivity, primarily dominated by the presence of complex-like defects.

The thermoelectric figure of merit zT of corresponding samples are displayed Fig. 9b. Note that zT values presented in this study are used to

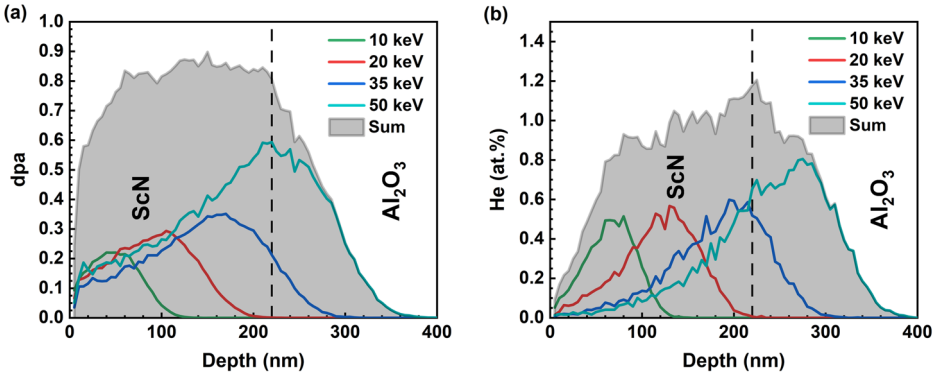

Fig. 10 | Simulation of the post-implantation defects and helium atom distribution in scandium nitride films. a Displacement per atom (dpa) and **b** concentration profiles as function of depth, calculated using SRIM code for a cumulative multi-energy He-1dpa implantation – 10 keV (green), 20 keV (red), 35 keV (dark blue), 50 keV (light blue) and the sum (gray).

compare the sample series and evaluate the relevance of the ion implantation and annealing conditions on the thermoelectric properties of ScN thin films. zT values are calculated from electrical properties that are measured in the in-plane direction while thermal conductivity measurements are performed in the cross-plane direction and most probably deviate from real values. Consequently, the absolute zT values must be taken with great care. However, the measurements being processed the same way for all samples, zT values can be compared. The implanted film experienced a 28% increased zT value with respect to the reference sample, owing to the large presence of defects which strongly reduce the thermal conductivity without reducing too much the power factor. As the PF is even greater for the sample annealed at 673 K, the zT further increased to an almost double value compared to the reference. The defects generated from a chemically inert He ion-implantation are thus sufficient to tune the transport properties in such a way that the overall thermoelectric performance is enhanced. On the other hand, an annealing at 1273 K induced a reduced power factor and recovered thermal conductivity, leading to a decreased zT value with respect to the reference. Therefore, a high temperature annealing (1273 K) of the He-implanted ScN films at 1 dpa is not beneficial for the thermoelectric performance of the films.

Conclusion

The structural and transport properties of ScN thin film deposited on Al_2O_3 substrates and implanted with chemically inert He ions were investigated for potential thermoelectric outcomes. A constant level of damage of 1 dpa was applied throughout the film to evaluate its impact on the properties, leading to a He concentration of about 1 at.%. TEM characterizations revealed the presence of interstitial clusters and nanocavities formed after agglomeration of He-vacancies complexes. Such cavities were present right after implantation, contrary to the Ar case, and were favorably formed in the grain boundary regions, thus following the same direction as that of the columnar grain growth. As high temperature annealing was performed, both structural and transport properties were affected, the transport being strongly dependent on the annealing temperature. Exhaustive investigation of the transport properties in each case revealed that the resistivity is manifold increased for all samples, mainly due to a strongly reduced mobility. The charge carrier concentration was reduced by half after implantation due to complex-like defects acting as trap carriers, releasing the electrons after their full recovery at 1273 K. That leads to a Seebeck coefficient identical to the reference sample, contrary to the implanted and 673 K annealed sample which exhibits about doubled Seebeck values. Consequently, the power factor was preserved for the sample annealed at 673 K, the rise of resistivity being compensated by the increased Seebeck coefficient. On the other hand, the thermal conductivity was strongly reduced for all samples, owing to defect clusters and nanocavities. That leads to significantly improved zT values, with a doubled value for the sample annealed at lower temperatures (673 K). This quite unexpected result appears truly promising as this technique can be applied to any low dimensional materials and thus opens a large window for improvement of any thermoelectric thin film. Taking advantage of chemically active species, it can be assumed that further transport properties optimization could be achieved by wisely choosing the nature of the doping ions and the implantation parameters. The ion implantation technique hence stands as a promising technique to improve the thermoelectric properties of state-of-the-art low dimensional materials.

Methods

Thin film growth and composition analysis

Epitaxial-like thin films of ScN were deposited using dc reactive magnetron sputtering in an ultra-high-vacuum chamber (base pressure 10^{-6} Pa), onto c-sapphire substrates maintained at 800 °C. The detailed deposition process and system is further described elsewhere[47,61]. The ScN films show a high electron concentration of about 10^{21} cm^{-3} due to the presence of unwanted oxygen impurities incorporated during deposition. Elastic recoil detection analysis (ERDA) characterizations were performed to assess the composition of the films, in particular determine the level of incorporation of any unwanted impurities. A 36 MeV ^{127}I beam was employed, with incident primary ions and recoiling species striking and exiting the sample at an angle of 67.5° to the surface normal, respectively. The Potku software package[62] was used to calculate the relative atomic concentration from the recorded ERDA spectra.

Implantation conditions

The 220 nm thick films were ion-implanted at room temperature using a EATON VN3206 implanter. The samples were characterized before implantation to allow comparison and assess the evolution of the structure and transport properties. The depth profiles of the implanted ions in the ScN films were simulated using SRIM 2013 software under the full-damage cascade[63]. A multi-energy implantation protocol was used to introduce a constant quantity of damage (called displacements per atom, noted dpa) as a function of the film depth. The level of dpa, in the range 0.8–1 dpa, was controlled by the fluences of incident ions. The energy profile extracted from SRIM 2013 simulations with helium ions is presented in Fig. 10, using four decreasing incident energies of 50, 35, 20 and 10 keV with fluences of 12×10^{15}, 6.4×10^{15}, 4.8×10^{15} and 3.2×10^{15} ions·cm^{-2}, respectively. These implantation parameters allow the introduction of a constant damage level into the film (reported as 1 dpa in the next sections for clarity), the concentration of helium atoms introduced fluctuating around 1 at.%. All implantation parameters are regrouped in Table 1.

Transport properties characterizations

The in-plane electrical resistivity ρ and charge carrier concentration n were measured in the Van der Pauw configuration using an ECOPIA HMS-5500 Hall measurement system in the 80–750 K temperature range. Hall measurements were performed using a constant magnetic field of 0.580 T. The carrier mobility was extracted using the relation $\mu = 1/ne\rho$, e being the elemental charge. The Seebeck coefficient was measured up to 680 K in a

classical linear four-probe configuration on a ULVAC ZEM3 apparatus using a thin film designed sample holder. High-temperature sample annealing was carried out in a home-made lamp furnace under vacuum during 10 min with a heating rate of about 20 °C.min^{-1}.

Transmission electron microscopy

TEM micrographs were obtained from a TALOS F200S Thermofisher microscope with a tension of 200 kV. Cross-section TEM samples were prepared on an FEI ThermoFisher Helios Nanolab 660 by using the standard lift-out technique. The thickness was then further reduced using a Precision Polishing Precision System (Gatan-PIPS) to reach sufficiently thin samples.

Thermal conductivity characterization

Modulated Thermo-Reflectance (MTR) microscopy characterizations were carried out to determine the thermal conductivity of the samples[64]. In this optical and non-destructive method, an intensity-modulated Laser (Pump) beam is focused on the surface of the sample (Objective X50 NA 0.5) at a frequency of 100 kHz, resulting in a modulated thermal response from the sample. Another probe Laser spatially scanning the sample measure its reflectance by fetching the signal back in a photodiode. The AC reflectance component recorded by a lock-in amplifier yields a signal characterized by a given amplitude and phase characteristic of the thermal properties of the sample. The probe beam signal is fitted by a multilayer thermal diffusion model, allowing the determination of the thermal conductivity and other thermal properties of the sample such as the specific heat and interfacial thermal resistance. The modulation frequency was set at 100 kHz. The wavelength of the pump and the probe Lasers were 532 and 488 nm, respectively. A thin transducer layer of gold was deposited on each sample (~60 nm) to maximize the probe's sensitivity to the thermal field.

The amplitudes and phases measured by MTR are leveraged to determine the thermal conductivity of all samples (Fig. 11). Clear differences can be observed between the samples, suggesting different thermal characteristics, consistent with both structural and electrical properties evolution described in the article. In particular, a broadening of both the amplitude and phase of the implanted sample is observed, which is consistent with a decreased thermal conductivity of the film layer.

As the sample was annealed, a recovery of both curves can be observed towards the reference ones, suggesting a recovery of the thermal conductivities. Detailed fittings of the curves were performed by a multi-layer model to accurately assess the thermal transport properties of the samples. Fitting curves according to this model applicated for the sample annealed at 1273 K is presented in Fig. 12. The measurements of all samples were fitted using the same method, considering the transducer layer (gold, ~60 nm thickness), the ScN film thickness (220 nm), the reduced thermal conductivity of the Al_2O_3 substrate near the interface, and all thermal resistance interfaces. The equivalent thermal resistance is defined as R_{eq} = thickness/thermal conductivity. In particular, the thermal resistance interface between the transducer layer and the ScN film was fixed as constant for all samples ($R_{eq} = 0.167 \times 10^{-8}$ m^2.K.W^{-1}). The thermal properties of the substrate were also considered as constant (with tabulated values of Al_2O_3). The two refined parameters were the thermal conductivity of ScN and the equivalent thermal resistance of the interface between ScN and the Al_2O_3 substrate. This choice can be explained by the fact that implantation of species into the substrate can lead to a decrease of the thermal conductivity of the substrate

Table. 1 | Parameters of multi-energy He ion-implantation into ScN thin films deposited on *c*-cut Al_2O_3 substrate obtained from SRIM simulations

Energy (keV)	R_p (nm)	ΔR_p (nm)	Skewness	V/ion	Fluence (cm^{-2})
50	245	63	−0.84	91	$12{\cdot}10^{15}$
35	183	54	−0.56	78	$6.4{\cdot}10^{15}$
20	116	41	−0.35	63	$4.8{\cdot}10^{15}$
10	64	26	−0.10	45	$3.2{\cdot}10^{15}$

Each distribution is characterized by the mean ion range R_p, straggling ΔR_p, and skewness. The V/ion ratio represents the number of vacancies generated by a single incident ion (simulations do not account for dynamic recombination processes). The fluence for each incident energy was calculated to achieve a final damage profile of 1 dpa (Displacements Per Atom).

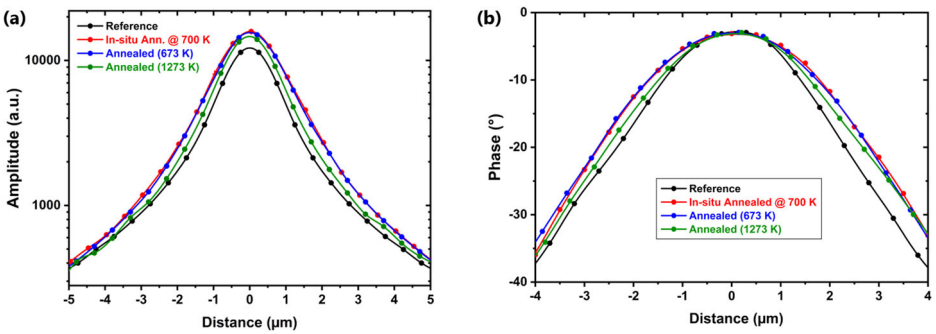

Fig. 11 | Modulated thermoreflectance signals of helium-implanted films annealed under different conditions. a Amplitudes and **b** phases of modulated thermoreflectance measurements performed on the ScN Reference, as-implanted, implanted then annealed at 673 K, and implanted then annealed at 1273 K films.

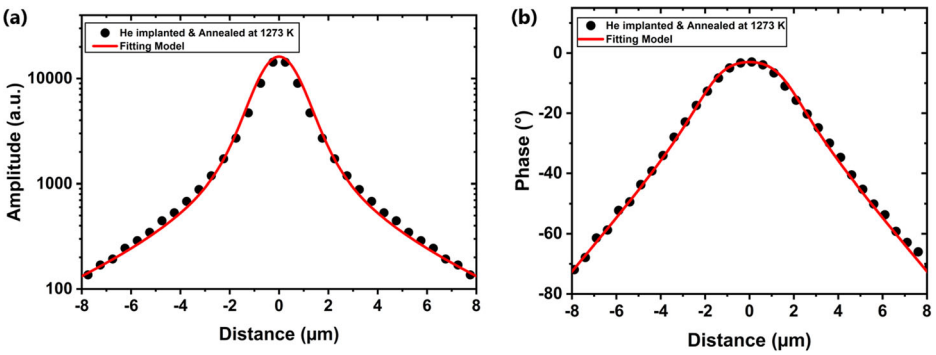

Fig. 12 | Fitted models of the measured signal of a helium-implanted scandium nitride film annealed at 1273 K. Fitting of the amplitude (**a**) and phase (**b**) of the modulated thermoreflectance signal by a multilayered model of the He-implanted sample annealed at 1273 K. Model: Transducer Au 50 nm ($R_{eq} = 0.167\ 10^{-8}$ m^2.K.W^{-1}); ScN film 220 nm ($R_{eq} = 2.00\ 10^{-8}$ m^2.K.W^{-1}); Al_2O_3 Interface 200 nm ($R_{eq} = 3.75\ 10^{-8}$ m^2.K.W^{-1}); Al_2O_3 substrate 500 μm, $\kappa = 46$ W.m^{-1}.K^{-1}.

in the region close to the film (about 100 nm), thus having a significant impact on the measured amplitude and phase of the modulated signal. Fittings of both amplitude and phase led to the determination of the ScN thermal conductivity and ScN/Al_2O_3 equivalent thermal resistance. The electronic contribution to the thermal conductivity was estimated using the Franz-Wiedemann law.

Data availability

The data that support the findings of this study are available from the corresponding author upon reasonable request.

Received: 22 July 2024; Accepted: 17 January 2025;
Published online: 15 February 2025

References

1. Ningthoujam, R. S. & Gajbhiye, N. S. Synthesis, Electron Transport Properties of Transition Metal Nitrides and Applications. *Prog. Mater. Sci.* **70**, 50–154 (2015).
2. Navinsek, B. & Seal, S. Transition Metal Nitride Functional Coatings. *JOM* **53**, 51–54 (2001).
3. Xie, J. & Xie, Y. Transition Metal Nitrides for Electrocatalytic Energy Conversion: Opportunities and Challenges. *Chem. Eur. J.* **22**, 3588–3598 (2016).
4. Wang, H. et al. Transition Metal Nitrides for Electrochemical Energy Applications. *Chem. Soc. Rev.* **50**, 1354–1390 (2021).
5. Peng, X. et al. Recent Progress of Transition Metal Nitrides for Efficient Electrocatalytic Water Splitting. *Sustain. Energy Fuels* **3**, 366–381 (2019).
6. Kindlund, H., Sangiovanni, D. G., Petrov, I., Greene, J. E. & Hultman, L. A Review of the *Intrinsic* Ductility and Toughness of Hard Transition-Metal Nitride Alloy Thin Films. *Thin Solid Films* **688**, 137479 (2019).
7. Lévy, F. et al. Electronic States and Mechanical Properties in Transition Metal Nitrides. *Surf. Coat. Technol.* **120–121**, 284–290 (1999).
8. Guler, U., Shalaev, V. M. & Boltasseva, A. Nanoparticle Plasmonics: Going Practical with Transition Metal Nitrides. *Mater. Today* **18**, 227–237 (2015).
9. Guler, U., Kildishev, A. V., Boltasseva, A. & Shalaev, V. M. Plasmonics on the Slope of Enlightenment: The Role of Transition Metal Nitrides. *Faraday Discuss* **178**, 71–86 (2015).
10. Zha, X.-H., Ma, X., Luo, J.-T. & Fu, C. Enhanced Piezoelectric Response of AlN via Alloying of Transitional Metals, and Influence of Type and Distribution of Transition Metals. *Nano Energy* **111**, 108390 (2023).
11. Eklund, P., Kerdsongpanya, S. & Alling, B. Transition-Metal-Nitride-Based Thin Films as Novel Energy Harvesting Materials. *J. Mater. Chem. C* **4**, 3905–3914 (2016).
12. Ohkubo, I. & Mori, T. Two-Dimensional Layered Complex Nitrides as a New Class of Thermoelectric Materials. *Chem. Mater.* **26**, 2532–2536 (2014).
13. Kerdsongpanya, S. et al. Anomalously High Thermoelectric Power Factor in Epitaxial ScN Thin Films. *Appl. Phys. Lett.* **99**, 232113 (2011).
14. Lambrecht, W. R. L. Electronic Structure and Optical Spectra of the Semimetal ScAs and of the Indirect-Band-Gap Semiconductors ScN and GdN. *Phys. Rev. B* **62**, 13538–13545 (2000).
15. Bai, X. & Kordesch, M. E. Structure and Optical Properties of ScN Thin Films. *Appl. Surf. Sci.* **175–176**, 499–504 (2001).
16. Stampfl, C., Mannstadt, W., Asahi, R. & Freeman, A. J. Electronic Structure and Physical Properties of Early Transition Metal Mononitrides: Density-Functional Theory LDA, GGA, and Screened-Exchange LDA FLAPW Calculations. *Phys. Rev. B* **63**, 155106 (2001).
17. Qteish, A., Rinke, P., Scheffler, M. & Neugebauer, J. Exact-Exchange-Based Quasiparticle Energy Calculations for the Band Gap, Effective Masses, and Deformation Potentials of ScN. *Phys. Rev. B* **74**, 245208 (2006).
18. Saha, B., Acharya, J., Sands, T. D. & Waghmare, U. V. Electronic Structure, Phonons, and Thermal Properties of ScN, ZrN, and HfN: A First-Principles Study. *J. Appl. Phys.* **107**, 033715 (2010).
19. Saha, B. et al. Electronic and Optical Properties of ScN and (Sc,Mn)N Thin Films Deposited by Reactive DC-Magnetron Sputtering. *J. Appl. Phys.* **114**, 063519 (2013).
20. Gall, D. et al. Growth of Poly- and Single-Crystal ScN on MgO(001): Role of Low-Energy N^{2+} Irradiation in Determining Texture, Microstructure Evolution, and Mechanical Properties. *J. Appl. Phys.* **84**, 6034–6041 (1998).
21. Saha, B., Shakouri, A. & Sands, T. D. Rocksalt Nitride Metal/Semiconductor Superlattices: A New Class of Artificially Structured Materials. *Appl. Phys. Rev.* **5**, 021101 (2018).
22. Biswas, B. & Saha, B. Development of Semiconducting ScN. *Phys. Rev. Mater.* **3**, 020301 (2019).
23. Kerdsongpanya, S. et al. Experimental and Theoretical Investigation of $Cr_{1-x}Sc_xN$ Solid Solutions for Thermoelectrics. *J. Appl. Phys.* **120**, 215103 (2016).
24. Kumagai, Y., Tsunoda, N. & Oba, F. Point Defects and p-Type Doping in ScN from First Principles. *Phys. Rev. Appl.* **9**, 034019 (2018).
25. Nayak, S. et al. Rigid-Band Electronic Structure of Scandium Nitride across the n-Type to p-Type Carrier Transition Regime. *Phys. Rev. B* **99**, 161117 (2019).
26. le Febvrier, A., Tureson, N., Stilkerich, N., Greczynski, G. & Eklund, P. Effect of Impurities on Morphology, Growth Mode, and Thermoelectric Properties of (1 1 1) and (0 0 1) Epitaxial-like ScN Films. *J. Phys. Appl. Phys.* **52**, 035302 (2018).
27. Rao, D. et al. High Mobility and High Thermoelectric Power Factor in Epitaxial ScN Thin Films Deposited with Plasma-Assisted Molecular Beam Epitaxy. *Appl. Phys. Lett.* **116**, 152103 (2020).
28. Burmistrova, P. V. et al. Effect of Deposition Pressure on the Microstructure and Thermoelectric Properties of Epitaxial ScN(001) Thin Films Sputtered onto MgO(001) Substrates. *J. Mater. Res.* **30**, 626–634 (2015).
29. Saha, B. et al. Compensation of Native Donor Doping in ScN: Carrier Concentration Control and p-Type ScN. *Appl. Phys. Lett.* **110**, 252104 (2017).
30. Saha, B. et al. Temperature-Dependent Thermal and Thermoelectric Properties of n-Type and p-Type $Sc_{1-x}Mg_xN$. *Phys. Rev. B* **97**, 085301 (2018).
31. Burmistrova, P. V. et al. Thermoelectric Properties of Epitaxial ScN Films Deposited by Reactive Magnetron Sputtering onto MgO(001) Substrates. *J. Appl. Phys.* **113**, 153704 (2013).
32. Snyder, G. J. & Toberer, E. S. Complex Thermoelectric Materials. *Nat. Mater.* **7**, 105–114 (2008).
33. Tang, X., Li, Z., Liu, W., Zhang, Q. & Uher, C. A Comprehensive Review on Bi_2Te_3-Based Thin Films: Thermoelectrics and Beyond. *Interdiscip. Mater.* **1**, 88–115 (2022).
34. Sootsman, J. R. et al. Large Enhancements in the Thermoelectric Power Factor of Bulk PbTe at High Temperature by Synergistic Nanostructuring. *Angew. Chem. Int. Ed.* **47**, 8618–8622 (2008).
35. Wei, J. et al. Review of Current High-ZT Thermoelectric Materials. *J. Mater. Sci.* **55**, 12642–12704 (2020).
36. Tureson, N. et al. Reduction of the Thermal Conductivity of the Thermoelectric Material ScN by Nb Alloying. *J. Appl. Phys.* **122**, 025116 (2017).
37. Zhao, Y. et al. Engineering the Thermal Conductivity along an Individual Silicon Nanowire by Selective Helium Ion Irradiation. *Nat. Commun.* **8**, 15919 (2017).
38. Wang, S., Xiao, Y., Chen, Q. & Hao, Q. Engineering Thermal Transport within Si Thin Films: The Impact of Nanoslot Alignment and Ion Implantation. *iScience* **25**, 105386 (2022).

39. Masarrat, A. et al. Effect of Fe Ion Implantation on the Thermoelectric Properties and Electronic Structures of $CoSb_3$ Thin Films. *RSC Adv* **9**, 36113–36122 (2019).
40. Bala, M. et al. Enhancement of Thermoelectric Power of PbTe Thin Films by Ag Ion Implantation. *J. Appl. Phys.* **121**, 215301 (2017).
41. Ahmad, B. et al. Enhancement of Thermoelectrical Performance in Au-Ion Implanted V_2O_5 Thin Films. *RSC Adv* **7**, 50648–50656 (2017).
42. Timm, M. M. et al. Ion Implantation Effects on the Microstructure, Electrical Resistivity and Thermal Conductivity of Amorphous $CrSi_2$ Thin Films. *J. Mater. Sci.* **57**, 1174–1185 (2022).
43. Kennedy, J., Murmu, P. P., Kumar, P. & Ramanath, G. Multifold Enhancements in Thermoelectric Power Factor in Isovalent Sulfur Doped Bismuth Antimony Telluride Films. *Mater. Res. Bull.* **142**, 111426 (2021).
44. Bhogra, A. et al. Tuning the Electrical and Thermoelectric Properties of N Ion Implanted $SrTiO_3$ Thin Films and Their Conduction Mechanisms. *Sci. Rep.* **9**, 1–11 (2019).
45. Burcea, R. et al. Influence of Generated Defects by Ar Implantation on the Thermoelectric Properties of ScN. *ACS Appl. Energy Mater.* **5**, 11025–11033 (2022).
46. Rao, D. et al. Multifunctional Irradiation-Induced Defects for Enhancing Thermoelectric Properties of Scandium Nitride Thin Films. *ACS Appl. Energy Mater.* **5**, 6847–6854 (2022).
47. Tureson, N. et al. Effect of Ion-Implantation-Induced Defects and Mg Dopants on the Thermoelectric Properties of ScN. *Phys. Rev. B* **98**, 205307 (2018).
48. Burcea, R. et al. Effect of Induced Defects on Conduction Mechanisms of Noble-Gas-Implanted ScN Thin Films. *J. Appl. Phys.* **134**, 055107 (2023).
49. Donnelly, S. E. & Evans, J. H., eds. *Fundamental Aspects of Inert Gases in Solids*. NATO ASI Series, vol. 279 (Springer, 1991). https://doi.org/10.1007/978-1-4899−3680-6.
50. Raineri, V., Saggio, M. & Rimini, E. Voids in Silicon by He Implantation: From Basic to Applications. *J. Mater. Res.* **15**, 1449–1477 (2000).
51. Fleischer, E. L. & M. G. Noble, Norton Gas Inclusions in Materials. *Heterog. Chem. Rev.* **3**, 171–201 (1996).
52. Mott, N. F., Davis, E. A., Mott, N. F. & Davis, E. A. *Electronic Processes in Non-Crystalline Materials; Oxford Classic Texts in the Physical Sciences* (Oxford University Press, 2012).
53. Mu, S., Rowberg, A. J. E., Leveillee, J., Giustino, F. & Van de Walle, C. G. First-Principles Study of Electron Transport in ScN. *Phys. Rev. B* **104**, 075118 (2021).
54. Shklovskii, B. I., Efros, A. L. *Electronic Properties of Doped Semiconductors*, Softcover reprint of the original 1st ed. 1984 ed. (Springer, 2012).
55. Pizzagalli, L., Charaf-Eddin, A. & Brochard, S. Numerical Simulations and Modeling of the Stability of Noble Gas Atoms in Interaction with Vacancies in Silicon. *Comput. Mater. Sci.* **95**, 149–158 (2014).
56. Toberer, E. S., Baranowski, L. L. & Dames, C. Advances in Thermal Conductivity. *Annu. Rev. Mater. Res.* **42**, 179–209 (2012).
57. Rudra, S., Rao, D., Poncé, S., & Saha, B. Dominant Scattering Mechanisms in Limiting the Electron Mobility of Scandium Nitride. *Nano Lett*. https://doi.org/10.1021/acs.nanolett.4c02920 (2024).
58. Xu, D., Tang, S., Du, X. & Hao, Q. Detecting the Major Charge-Carrier Scattering Mechanism in Graphene Antidot Lattices. *Carbon* **144**, 601–607 (2019).
59. Suh, J. et al. Simultaneous Enhancement of Electrical Conductivity and Thermopower of Bi_2Te_3 by Multifunctionality of Native Defects. *Adv. Mater.* **27**, 3681–3686 (2015).
60. Zheng, Y. et al. Defect Engineering in Thermoelectric Materials: What Have We Learned? *Chem. Soc. Rev.* **50**, 9022–9054 (2021).
61. le Febvrier, A. et al. An Upgraded Ultra-High Vacuum Magnetron-Sputtering System for High-Versatility and Software-Controlled Deposition. *Vacuum* **187**, 110137 (2021).
62. Arstila, K. et al. Potku – New Analysis Software for Heavy Ion Elastic Recoil Detection Analysis. *Nucl. Instrum. Methods Phys. Res. Sect. B Beam Interact. Mater.* **331**, 34–41 (2014).
63. Ziegler, J. F., Ziegler, M. D. & Biersack, J. P. SRIM – The Stopping and Range of Ions in Matter (2010). *Nucl. Instrum. Methods Phys. Res. Sect. B Beam Interact. Mater.* **268**, 1818–1823 (2010).
64. Fournier, D., Marangolo, M. & Fretigny, C. Measurement of Thermal Properties of Bulk Materials and Thin Films by Modulated Thermoreflectance (MTR). *J. Appl. Phys.* **128**, 241101 (2020).

Acknowledgements

Dominique Eyidi is acknowledged for his assistance regarding TEM characterizations. This work was supported by the French government program "Investissements d'Avenir" (EUR INTREE – reference ANR-18-EURE-0010, LABEX INTERACTIFS – reference ANR-11-LABEX-0017-01, and UP-SQUARED – reference ANR-21-EXES-0013). The authors also acknowledge funding from the Swedish Research Council (VR) under Project No. 2021-03826, the Knut and Alice Wallenberg Foundation through the Wallenberg Academy Fellows program (grant no. KAW 2020.0196), the Swedish Government Strategic Research Area in Materials Science on Functional Materials at Linköping University (Faculty Grant SFO-Mat-LiU No. 2009 00971), and the Swedish Energy Agency under project 46519-1. Accelerator operation was supported by Swedish Research Council VR-RFI (Contract No. 2019-00191).

Author contributions

H.B.: Conceptualization, Validation, Formal Analysis, Data Curation, Investigation, Visualization, Writing – Original Draft; R.B.: Conceptualization, Methodology, Validation, Formal Analysis, Data Curation, Investigation, Visualization, Writing – Review & Editing; C.P.: Validation, Investigation, Data Curation, Visualization; D.F.: Validation, Formal Analysis, Investigation, Resources, Data Curation; F.G.: Investigation, Resources; J.N.: Investigation, Resources; Y. E.: Validation, Funding Acquisition; S. D.: Validation, Supervision, Funding Acquisition, Writing – Review & Editing; P.E.: Validation, Supervision, Funding Acquisition, Resources, Writing – Review & Editing; A.LF.: Validation, Formal Analysis, Investigation, Supervision, Funding Acquisition, Resources, Project Administration, Writing – Review & Editing; J-F.B.: Conceptualization, Methodology, Validation, Formal Analysis, Investigation, Supervision, Funding Acquisition, Resources, Project Administration, Writing – Review & Editing.

Funding

Open access funding provided by Uppsala University.

Competing interests

The authors declare no competing interests.

Additional information

Supplementary information The online version contains supplementary material available at https://doi.org/10.1038/s43246-025-00741-2.

Correspondence and requests for materials should be addressed to Hugo Bouteiller, Arnaud le Febvrier or Jean-François Barbot.

Peer review information *Communications Materials* thanks the anonymous reviewers for their contribution to the peer review of this work. Primary Handling Editors: Yanzhong Pei and Jet-Sing Lee. A peer review file is available.